

PCCP

Accepted Manuscript



This is an *Accepted Manuscript*, which has been through the Royal Society of Chemistry peer review process and has been accepted for publication.

Accepted Manuscripts are published online shortly after acceptance, before technical editing, formatting and proof reading. Using this free service, authors can make their results available to the community, in citable form, before we publish the edited article. We will replace this *Accepted Manuscript* with the edited and formatted *Advance Article* as soon as it is available.

You can find more information about *Accepted Manuscripts* in the [Information for Authors](#).

Please note that technical editing may introduce minor changes to the text and/or graphics, which may alter content. The journal's standard [Terms & Conditions](#) and the [Ethical guidelines](#) still apply. In no event shall the Royal Society of Chemistry be held responsible for any errors or omissions in this *Accepted Manuscript* or any consequences arising from the use of any information it contains.

Mechanical Properties of Mesoporous Ceria Nanoarchitectures

Thi X. T. Sayle¹, Beverly Inkson², Günter Möbus², Stephen C. Parker³, Sudipta Seal^{4,5,6} and Dean C. Sayle^{1,*}

¹School of Physical Sciences, University of Kent, Canterbury, CT2 7NZ, UK *d.c.sayle@kent.ac.uk

²NanoLAB Centre, Dept. of Materials Science and Engineering, Sheffield University, Sheffield, S1 3JD, UK

³Dept. of Chemistry, University of Bath, Claverton Down, Bath, Avon, BA2 7AY, UK

⁴Advanced Materials Processing and Analysis Center, University of Central Florida, Orlando, FL-32816, USA

⁵NanoScience Technology Center, University of Central Florida, Orlando, FL-32816, USA

⁶Mechanical Materials and Aerospace Engineering, University of Central Florida, Orlando, FL-32816, USA

ABSTRACT

Architectural constructs are engineered to impart desirable mechanical properties facilitating bridges, spanning a thousand meters and buildings nearly 1km in height. However, do the same 'engineering-rules' translate to the nanoscale, where the architectural features are less than 0.0001 mm in size? Here, we calculate the mechanical properties of a porous ceramic functional material, ceria, as a function of its nanoarchitecture using molecular dynamics simulation and predict its yield strength to be almost two orders of magnitude higher than the parent bulk material. In particular, we generate models of nanoporous ceria with either a hexagonal or cubic array of one-dimensional pores and simulate their responses to mechanical load. We find that the mechanical properties are critically dependent upon the orientation between the crystal structure (symmetry, direction) and the pore structure (symmetry, direction).

INTRODUCTION

The architecture of a bridge plays a pivotal role with respect to its load bearing capability - as exemplified by the arch construct, which has been exploited for over 4000 years. Nature also exploits complex architectures to facilitate high mechanical strength coupled with light-weight design. However, many man-made materials are metals and are fully dense, which are atypical of the materials found naturally; rather nature exploits ceramic materials to communicate 'strength' including, for example, bone (apatite) or shell (carbonate).^[1] It is therefore prudent to consider how one might copy nature and explore architectures that proffer desirable mechanical strength yet are light-weight. Indeed, Lai and co-workers replicated the remarkable form of a sea urchin skeletal plate to form macroporous copper with a triply periodic minimal surface and superior mechanical properties ^[2].

The exemplary mechanical properties of a ceramic, such as hardness, elastic moduli are difficult to exploit because of the associated brittleness and low fracture toughness. However, hierarchical structural control can be used to engineer materials, which can sustain elastic deformation up to 10% ^[3], spawning the emerging field of 'ultra-strength' materials ^[4].

The challenge is to manufacture ceramics with macroscopic dimensions yet retain architectural features at the nanoscale, which modify the mechanical properties in a beneficial way. Jauffres and co-workers found that macroporous ceramic films, under mechanical load, present a very short elastic deformation, followed by brittle collapse. Conversely, nanoporous ceramics displayed contrasting behaviour with 'classical elastoplastic deformation and significant elastic recovery' ^[5]. For nanoporous materials, the evolution of cracks and dislocations are frustrated because they can potentially be annihilating at free surfaces, which may be only nanometers away.

In addition, nanoporous materials, with a nanoframe of smaller relative density than the fully dense parent material, can dissipate more energy per volume because the geometry of the nanoframe evolves during deformation to engage more of the material in plastic deformation ^[6]. This is because the void space within the porous material provides additional degrees of freedom to facilitate such geometrical evolution. Nanoporous

ceramics enjoy such attributes and can be manufactured with controllable nanoarchitectures [7]. It is therefore pertinent to explore whether architectures, such as the arch construct, can be exploited at the nanoscale to proffer desirable mechanical properties – a first step in unravelling ‘engineering rules at the nanoscale’.

Nanoporous functional materials are exploited in a wide variety of applications including: catalysis, energy conversion (battery, fuel cell), sensors [8], adsorption and separation [7] and are being synthesised with ever increasing nanoarchitectural complexity including pores traversing zero-, one-, two- and three-dimensions that may, or may not be interconnecting; bimodal and trimodal have also been synthesised [7]. However, under normal operating conditions, mechanical loading from, for example, friction and wear, thermal stress, mechanical stress and mechanical/thermal fatigue may reduce the lifespan of the material. It is therefore desirable to understand their mechanical properties such that they can be manufactured with improved durability. Here, we use atomistic computer simulation to start to understand how the nanoarchitecture impacts upon the mechanical properties. Specifically, as a first step, we predict the mechanical strength of a nanoporous functional oxide, ceria, with either a hexagonal or cubic array of 1D pores.

METHODS

In this section we outline the potential model used to describe the nanoporous ceria, the computer code used to perform the molecular dynamical simulations, the approach to generate full atomistic models of nanoporous ceria, which comprises complex microstructures, and the approach used to simulate deformation under uniaxial loading.

Potential Model All calculations, presented in this study, were based upon the Born model of the ionic solid, where the energy, E , of the system is given by:

$$E(r_{ij}) = \sum_{ij} \frac{Q_i Q_j}{4\pi\epsilon_0 r_{ij}} + \sum_{ij} A \exp\left(\frac{-r_{ij}}{\rho}\right) - C r_{ij}^{-6},$$

the first term represents the Coulombic interaction between ion i of charge Q_i and ion j of charge Q_j , which are a distance r_{ij} apart. The second term is of the Buckingham form, which

is particularly effective in representing ionic solids. Model parameters were taken from ref [9].

Simulation Code The DL_POLY code, with three-dimensional periodic boundary conditions, was used to perform all the molecular dynamics (MD) simulations; the user manual provides comprehensive analytical descriptions and discussion of the molecular dynamics simulations, force fields, boundary conditions, algorithms and parallelisation methods used in these simulations [10].

Atomistic Model The mechanical properties of nanoporous ceria are influenced by three levels of hierarchical structural complexity: crystal structure, microstructure (grain-boundaries, dislocations, point defects) and pore structure (symmetry, size, shape and connectivity of internal pores). Accordingly, if simulation is to generate models of nanoporous ceria, which can be interrogated to reliably predict mechanical properties, then all these levels of structural complexity must be included within a (single) atomistic model. Experimentally, hierarchical structural complexity evolves during self-assembly and crystallisation. Intuitively, by simulating these processes, such hierarchical structural models can be generated. Here, we simulate the synthetic protocol of Deshpande and co-workers who used 'CeO₂ nanoparticles as building blocks in a block-copolymer-assisted assembly process to obtain nanoporous materials' [11]. In particular, we generate amorphous nanoparticles of ceria, position them within a simulation cell with either cubic or hexagonal symmetry, and allow the nanoparticles to agglomerate together to yield a continuous nanoporous network. The amorphous ceria, comprising the framework architectures, is then crystallised.

Specifically, a cube of CeO₂, comprising 15972 ions, was cleaved from the parent bulk material, fig. 1(a) and amorphised by performing MD simulation at 8000K for 50ps, fig 1(b,c). The nanoparticle was then positioned within either a cubic or hexagonal simulation cell to facilitate nanoarchitectures with either a cubic or hexagonal array of 1-D pores, fig 1(d,e).

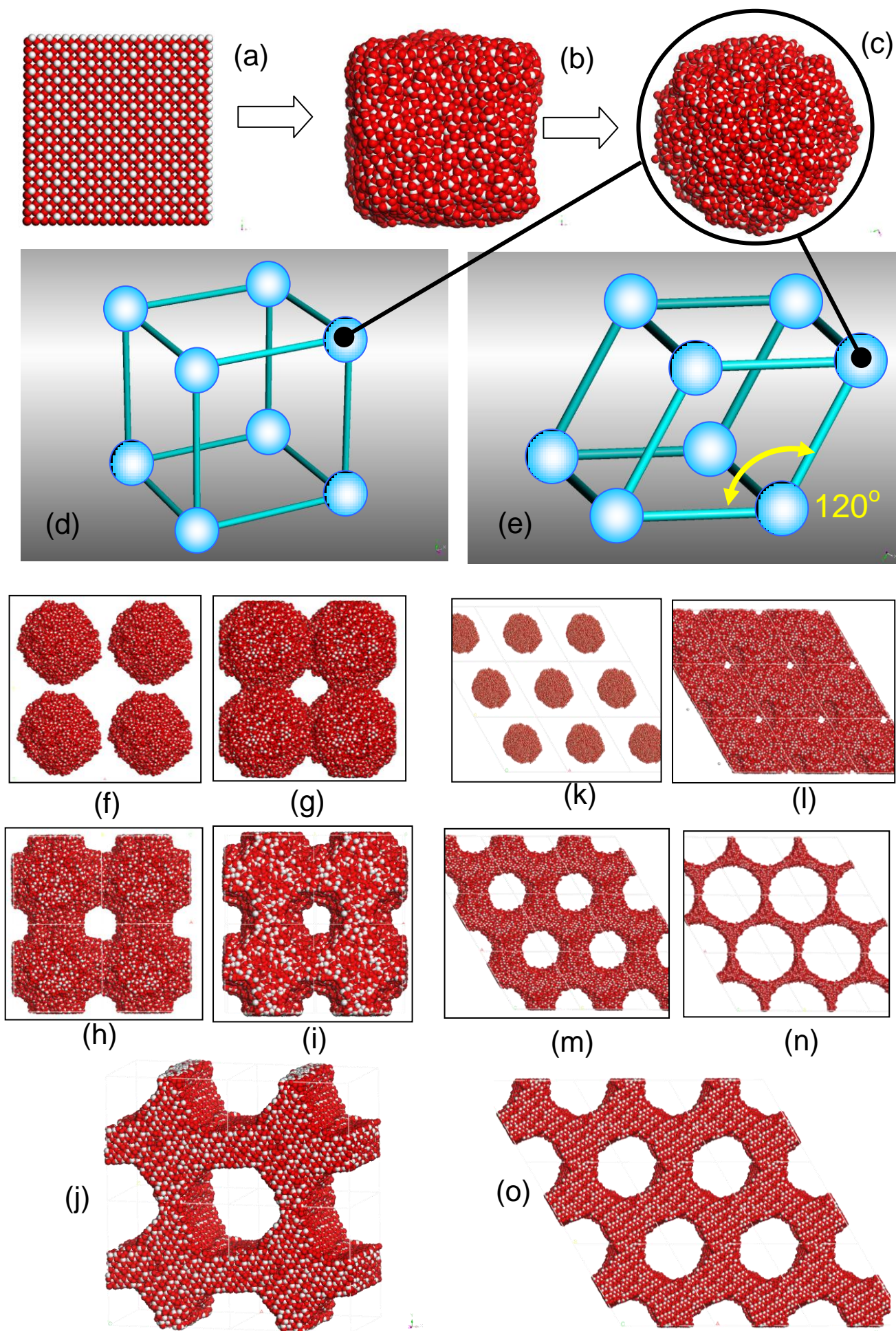


Figure 1 Generating atomistic models of nanoporous architectures. (a) A nanoparticle is cleaved from the parent material and is amorphised (b,c) and positioned at lattice points within a cubic (d) or hexagonal (e) simulation cell. The nanoparticles are allowed to agglomerate together to facilitate a cubic (f,g) or hexagonal (k,l) array of 1D pores respectively. Once agglomerated, the simulation cell is expanded until the desired wall thickness is achieved (h,i) and (m,n). Finally, the systems are crystallised to facilitate the models for nanoporous ceria with cubic, (j), or hexagonal, (o), array of 1D pores. Cerium atoms are represented by the white spheres and oxygen, red spheres.

To evolve the pores, constant pressure MD simulation was performed at 8000K with a slight positive pressure to encourage the nanoparticles to agglomerate with their periodic neighbours. Such agglomeration is shown for the cubic and hexagonal pore systems in fig 1(f-g) and fig (k-l) respectively. Once the nanoparticles had agglomerated, constant pressure MD simulation was performed at 8000K, with a slight negative pressure, to enlarge the diameter of the pores and thereby reduce the wall thickness, fig 1(h-i) and fig 1(m-n). We note that during MD performed at 8000K the CeO₂ remains in a molten state facilitating spherical pores as the system minimises its surface energy.

Once the desirable wall thickness was reached, the system was crystallised and then cooled to 0K. This was achieved by performing constant volume MD simulation at 3750K for typically 1000ps and at 0K for 50ps. Low temperature structures are shown in fig. 1(j,o).

The images, fig 1(m,n) show two snapshots of the simulation captured from the trajectory. As the simulation progressed, the wall thickness decreased. Accordingly, the trajectory file of the atom coordinates comprises atomistic models with a variety of wall thicknesses. The model chosen was the one with a wall thickness of 10nm, which is typically observed experimentally for mesoporous ceria.

For the system with a hexagonal array of 1-D pores, a dislocation spontaneously evolved during crystallisation. Accordingly, to explore the mechanical behaviour as influenced by the dislocation, we generated a further model by annealing out the dislocation. To achieve this, constant pressure MD simulation was performed at 4750K for 20,000ps during which time

the dislocation was annihilated at the internal surface. This result exemplifies how easy it is to annihilate dislocations in nanoporous materials with walls only 5nm thick. In particular, MD simulation can only simulate small windows in time and yet this was sufficient to annihilate the dislocation.

Deformation simulation

The mechanical properties of the nanoporous ceria were calculated by simulating stress-strain curves in response to applied uniaxial load. The elastic moduli were derived by calculating the gradient of the stress-strain curves and the yield strength was taken as the point on the stress-strain curve, where the curve showed a discontinuity.

Constant (uniaxial) Pressure simulations

Stress was introduced into the system by sequentially increasing the pressure along one direction and allowing the system to relax (zero pressure) in perpendicular directions using an NST ensemble (constant Number of particles, constant Stress and constant Temperature). In particular pressure increments of 0.01GPa were imposed followed by NST MD simulation performed at 300K for 5ps followed by a 5ps equilibration period, the latter helps mitigate the effect of the high strain rate. All models were first equilibrated by performing constant stress MD simulation at 300K for 100ps with a preliminary 25ps equilibration step.

RESULTS

In this section we describe the atomistic structures and mechanical properties of the nanoporous ceria.

Atomistic structures

The atomistic structures of nanoporous CeO₂ with hexagonal and cubic arrays of 1-D pores are shown in fig 2(a,b) and (c,d) respectively. Inspection of the models reveals that the pores have a pseudo hexagonal cross section; an enlarged view of the nanoceria with 1D hexagonal pores is shown in 1(e). Nanoporous ceria, synthesised via the assembly of ceria nanocrystals into highly ordered 3D nanostructures, reveal architectures similar to those of our atomistic models, 1(e) inset [11], and act as validation.

Herein, for ease of reference, we label the model nanoarchitectures as comprising ‘cubic’ or ‘hexagonal’ arrays of one-dimensional pores (fig 2(b), hexagonal, $x=y$, angle = 120° ; fig 2(d): cubic, $x=y$, angle = 90°). This is a somewhat disingenuous nomenclature because the crystallisation, as a consequence of the relationship between the pore structure and crystal structure (orientation), caused the cells to deviate from these high symmetry assignments. Moreover, as the results will reveal, the actual symmetry is pivotal to the properties of these nanoporous materials.

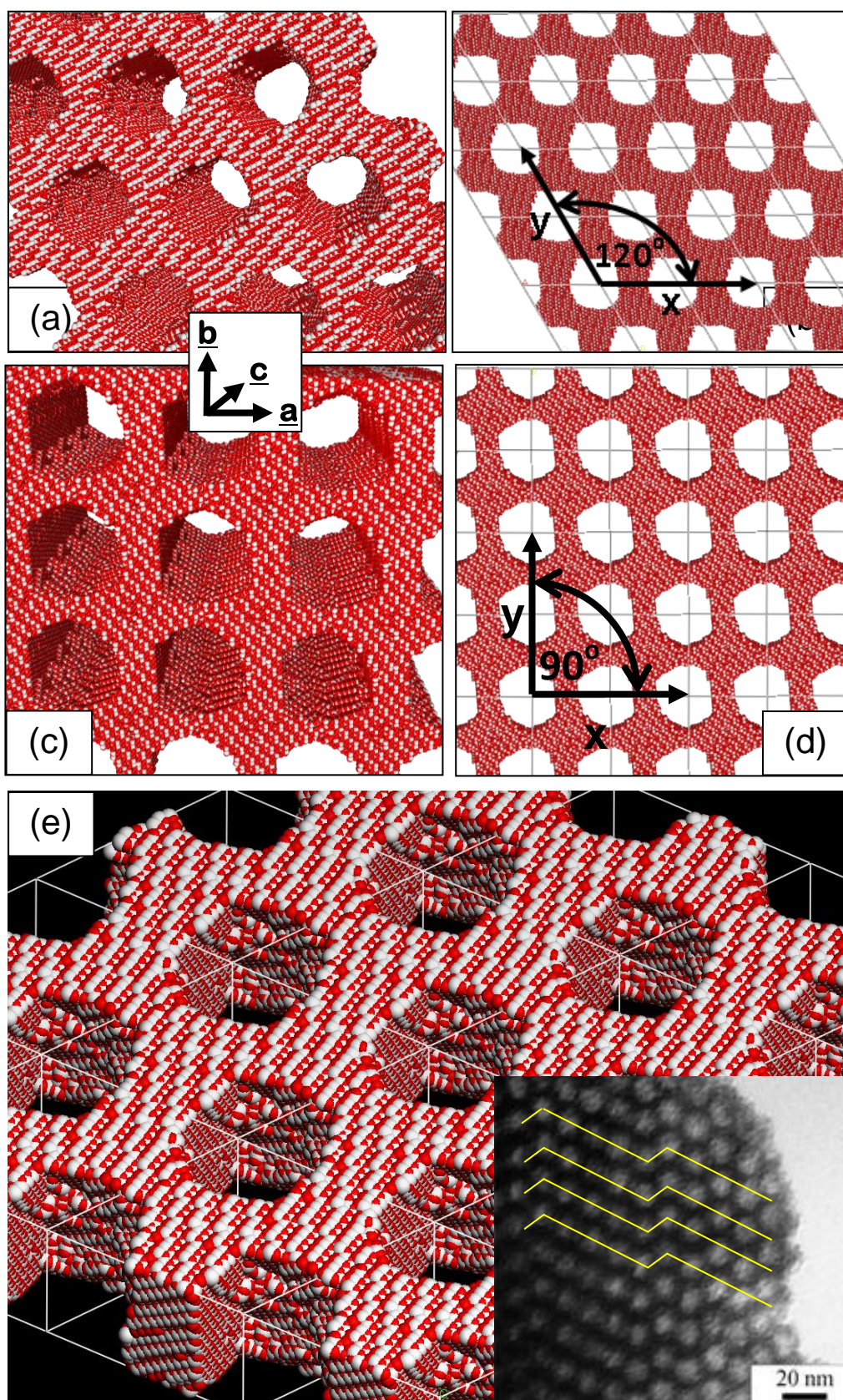
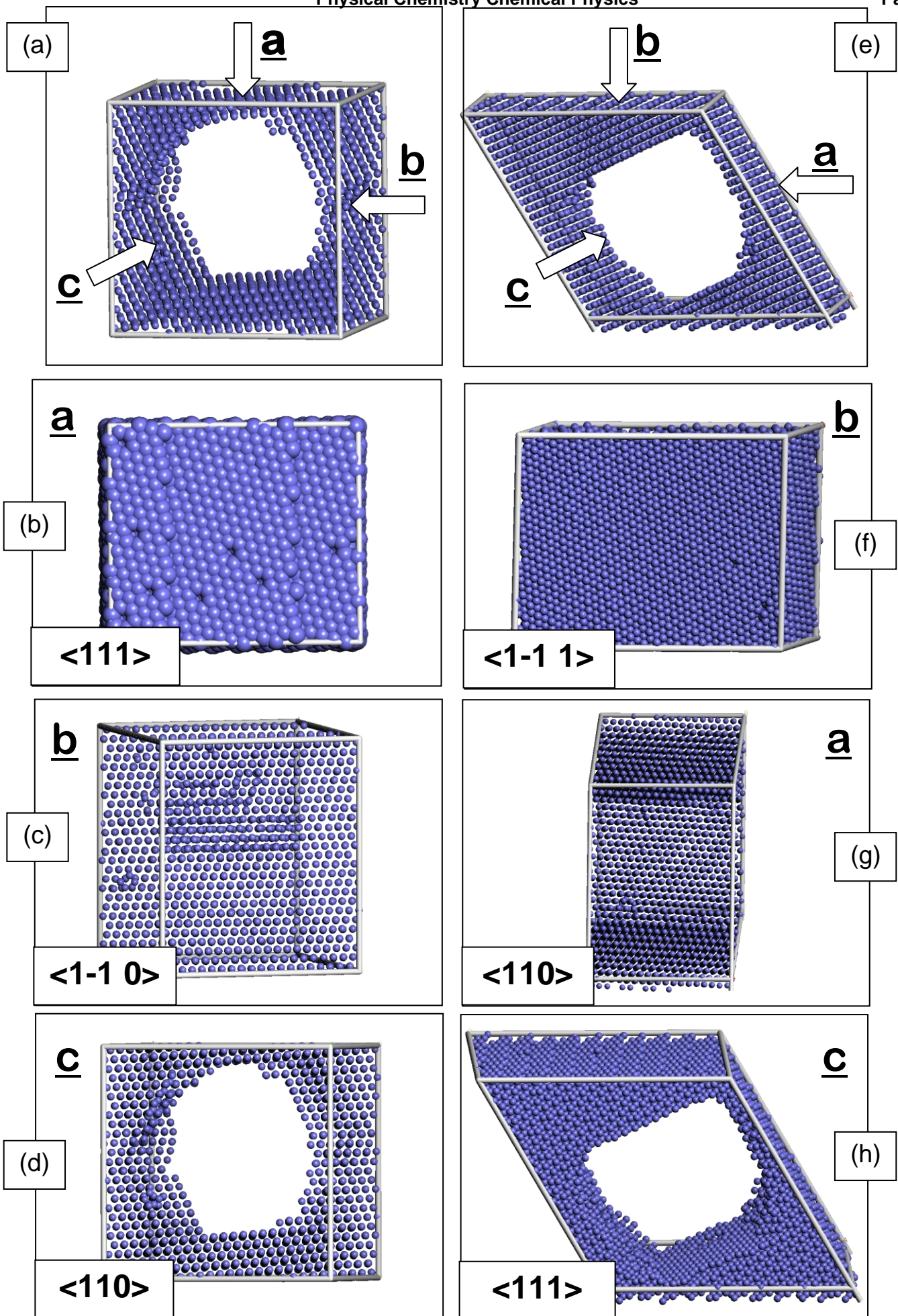


Figure 2 Sphere model representations of the atom positions comprising nanoporous ceria. (a) Perspective view of the system comprising a hexagonal array of pores. (b) View parallel to the hexagonal pore direction. (c) Perspective view and (d) view parallel to the cubic array of pores. The loading directions (**a**, **b**, **c**) are shown inset. (e) Enlarged view showing the hexagonal pores with hexagonal cross section compared with experiment (inset); the latter is taken, with permission from ref [11] Copyright © 2005 WILEY-VCH Verlag GmbH & Co. KGaA, Weinheim.

The crystal structure of a material is central to its mechanical properties; for materials with anisotropic crystal structures the elastic moduli will differ along the primary crystallographic axes. Similarly, we expect that the mechanical properties of nanoporous materials will differ if measured parallel or perpendicular to the pore directions. The mechanical anisotropy of the nanoporous material therefore rests critically upon the crystal structure and pore structure of the material and especially the orientational relationship between these two hierarchical levels of structure. Analysis of the atomistic models, using graphical techniques, reveals that the direction of the pores (which we have used to define the coordinate system along which compressive or tensile load is applied) is slightly off-axis to the major crystallographic directions of a fluorite structure, fig 3. For example, for the system comprising a cubic array of pores, the pore traverses along **c**, fig 3(a). However, fig 3(d) is drawn with the $\langle 110 \rangle$ crystal direction of the fluorite structure perpendicular to the page, which is slightly misaligned with respect to **c** (as evidenced by the rotation of the box in 3(d)). Similarly, for the system comprising a hexagonal array of pores, fig 3(e), the pore direction is along **c**. However, fig 3(h) is shown with the $\langle 111 \rangle$ crystal direction of the fluorite structure perpendicular to the page and is slightly misaligned with respect to **c**. The other load directions **a** and **b** are also slightly misaligned with respect to major crystal directions, figs 3(b,c) and figs 3(f,g).

It is important to understand how the (synergistic) relationship between crystal orientation and pore direction manifests as a first step in being able to exact control over this relationship to help facilitate tuneable mechanical properties.

Our simulations reveal that the origins of such orientational relationship rest with the crystalline nucleating seed, which spontaneously evolves exposing $\text{CeO}_2\{111\}$ at the surface, fig. 4. Exposure of this internal surface is energetically driven; $\text{CeO}_2(111)$ is the most stable surface of ceria [9]. However, the crystallographic orientation of the seed perpendicular to $\langle 111 \rangle$ and relative to the pore structure, is not thermodynamically driven because it is surrounded by an amorphous sea of ions; rather all orientations (rotational angles about $\langle 111 \rangle$) are thermodynamically equivalent. However, this angle, fig 4(a), governs the orientation of the crystal structure with respect to the pore structure. In particular, as the seed nucleates crystallisation of the surrounding sea of ions, navigating its way around the pore, the exposure of particular surfaces at the internal surfaces of the pore are dependent upon the orientation of the 'embryonic' crystalline seed with respect to the pore direction.



*Figure 3 Coordinate system (**a**, **b**, **c** directions – along which uniaxial compression or tension will be applied) with respect to the primary crystallographic directions of the nanoporous ceria. Cerium atom positions are shown as blue spheres; oxygen atoms are not shown to improve clarity. The images reveal that the coordinate system is off-axis compared to major crystallographic directions associated with the fluorite-structured ceria.*

Moreover, after circumnavigating the pore, the two crystallisation fronts must inevitably meet. It is unlikely that the two crystallisation fronts will be crystallographically aligned and therefore when they impinge upon one another a grain-boundary is formed. The situation is further complex because the relationship between the size of the pore with respect to the lattice parameter of ceria is likely incommensurate thus further frustrating the alignment of the crystallisation fronts. The necessity for imposing periodic boundary conditions will also introduce an 'artificial' constraint into the system as the crystallisation fronts impinge upon their images. Complete characterisation of these various phenomena is beyond the scope of this study. However, visualisation of the crystallisation process using graphical techniques, can provide qualitative insight and reveals considerable relaxation and rearrangement of atoms to low-energy positions, increasing the symmetry of the grain-boundaries. Performing the simulated crystallisations at high temperatures facilitates greatly the process and we observe a 'pseudo' Oswald ripening process with some grains being annealed out via growth and realignment at the grain-boundary regions. We also note that the porous structure enables additional relaxational freedom during crystallisation (into the void space) and facilitates strain mitigating within the lattice compared to the parent bulk material.

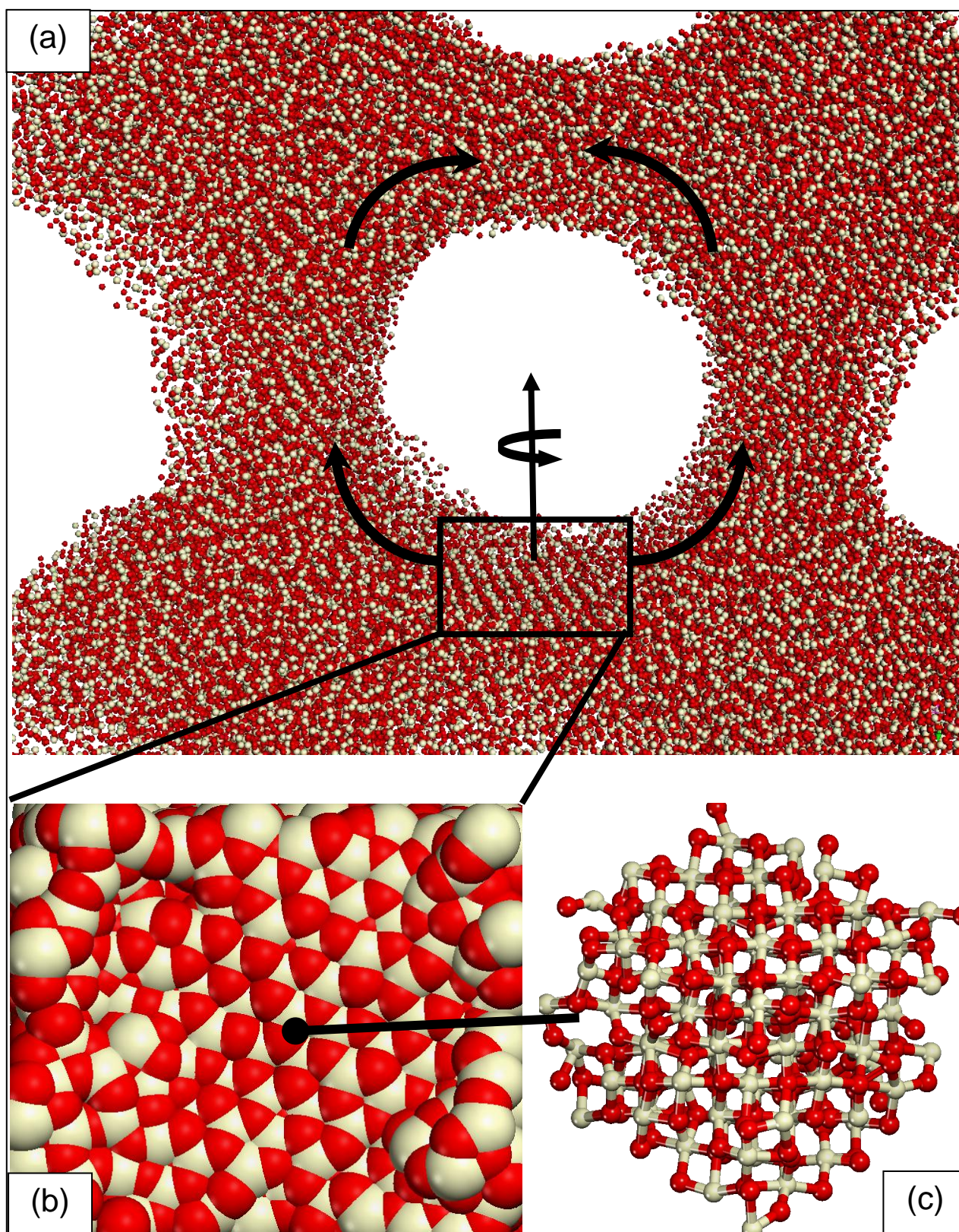


Figure 4 Embryonic stages of the nucleating seed evolution. (a) View parallel to the pore direction showing the crystalline seed, enclosed by the rectangle, surrounded by an amorphous sea of Ce and O ions. (b) View looking normal to the surface of the seed showing that it exposes the {111} at the internal pore surface. (c) Ball and stick model showing the ceria seed has crystallised into the fluorite polymorph. Cerium is coloured white and oxygen is red.

Cubic Pore System

Fig 5 shows the surfaces exposed within the pores for nanoporous ceria with a cubic array of 1D pores. A perspective view looking along the pore direction is shown in 5(a) and reveals a pseudo hexagonal pore shape cross-section with the top and bottom surfaces of the pore exposing {111} facets. We note that the crystal is missoriented with respect to the pore directions and therefore {111} of the crystal is (strictly) not perpendicular to the pore direction; rather it is vicinally aligned as evidenced by the steps on the {111} surfaces.

Nanoporous ceria has been synthesised using blockcopolymer templates and a non-aqueous solvent [12]. In particular, similar to the model structures, the real nanoporous material comprised crystalline walls with {111} planes exposed at the surfaces of the internal pores. The structural accord between the atomistic model, fig 5(a), and the real material, fig 5(b), helps validate the models and proffers confidence in using the models to interrogate the mechanical properties.

The other four surfaces (ceria model) are similar to {100}. Closer analysis using molecular graphics reveal that these {100} surfaces are, in part, {111} faceted. Such structural evolution is thermodynamically driven because $\text{CeO}_2\{111\}$ is energetically the most stable surface. In addition to the faceting, the {100} surfaces expose $-\text{O}-\text{Ce}-\text{O}-\text{Ce}-\text{O}-\text{Ce}-$ chains with CeO, rather than CeO_2 , stoichiometry at the surface, fig 5(c,d). This is because $\text{CeO}_2\{100\}$ is dipolar and therefore intrinsically unstable [9,13]. To facilitate stability of the $\text{CeO}_2\{100\}$ surfaces, the dipole perpendicular to the surface needs to be quenched, which is achieved by reducing the number of surface oxygen by 50% via the evolution of $-\text{O}-\text{Ce}-\text{O}-\text{Ce}-\text{O}-\text{Ce}-$

chain structures. The evolution of such structures occurs during the (simulated) crystallisation process.

Microstructure Analysis of the cubic pore system, using graphical techniques, reveals twin grain-boundaries with {111} interfacial planes. In particular, thin slices comprising three atomic layers cut through the wall of the porous architecture reveal 'A-B-A' stacking of the Ce sublattice at the boundary, compared with 'A-B-C' stacking further from the boundary plane, the latter is commensurate with the fluorite structure. We explore the implications of the grain-boundary in the section on mechanical properties.

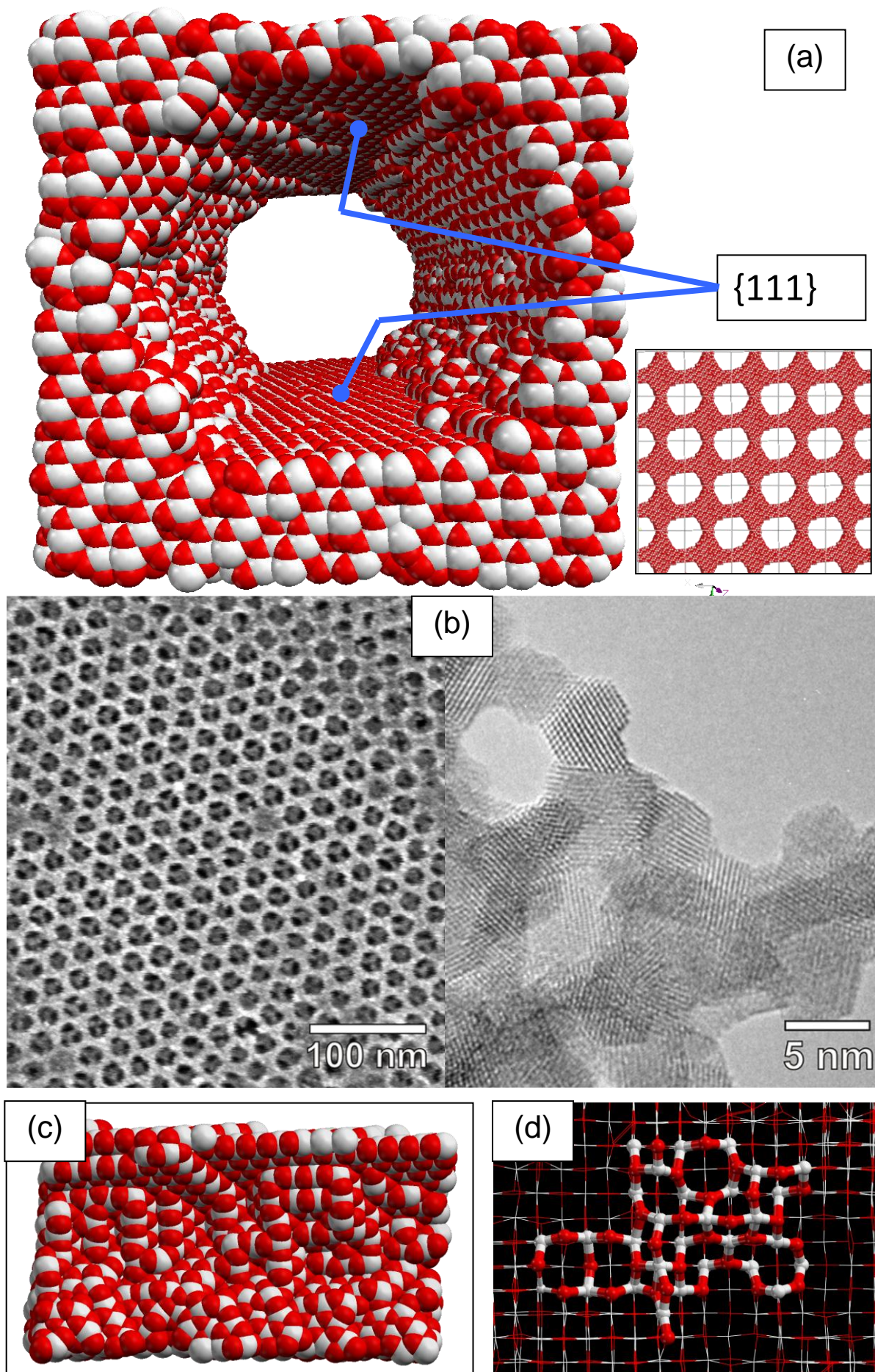


Figure 5 Characterisation of the internal pore surfaces of the ceria with a cubic array of pores. (a) Perspective view looking along one of the pores, which has a (pseudo) hexagonal cross-section with $\{111\}$ exposed at the top and bottom surfaces. (b) Comparison with real nanoporous ceria which also appears to expose $\{111\}$ at the pore surface [12]. Reproduced with permission from Ref. [12], Copyright (2013) American Chemical Society. (c) view showing one of the $\{100\}$ surfaces exposed by the pores. (d) Ball and stick representation of the atom positions comprising the uppermost atomic layer (and stick model for lower layers) showing CeO (as opposed to CeO₂) stoichiometry as a mechanism form quenching the dipole associated with CeO₂ $\{100\}$ -type III surfaces. Cerium is coloured white and oxygen is red.

Hexagonal Pore System

The atomistic structure of the pores in nanoporous ceria, comprising a hexagonal array of 1D pores, is shown in fig 6. Similar to the cubic pore system, the ceria crystallised to facilitate a hexagonal array of pores that expose $\{111\}$ at the top and bottom surfaces of the individual pores and a pseudo hexagonal pore cross-section. The other four surfaces exposed at the pore are heavily $\{111\}$ -faceted and comprise a wealth of steps edges and corners. Such faceting is shown more clearly in figs. 6(b, c, d). The morphology of step structures on the CeO₂ $\{111\}$ surface has been studied by dynamic scanning force microscopy and reveal topographical surface features similar to those of our atomistic models, fig. 6(e). We note a remarkable accord as show by the regions in the yellow ovals on the atomistic model, 6(d), and experiment, 6(e).

Microstructure Inspection of the model reveals that the hexagonal pore system comprises a screw-edge dislocation with Burgers vector similar to $\frac{1}{2}\langle 110 \rangle$, which traverses through the wall of the nanoporous ceria. The top and bottom surfaces of the wall comprising the screw-edge dislocation are shown in figs 7(a) and (b) respectively and the edge and screw components of the dislocation in 7(c) and 7(d) respectively. The dislocation facilitates steps on the surface of the pore wall, 7(a), which is enlarged in 7(e) to reveal a pit with steps exposing $\{100\}$ and $\{110\}$ 'nanofacets' with a step height of three atomic layers(O-Ce-O). Such structural features have been observed experimentally [14] and are shown in 7(f, g) to compare with the atomistic models; experimentally the steps are also three atomic layers in height.

That such surface defects, which have spontaneously evolved in the atomistic model during crystallization, are observed experimentally, helps validate the atomistic model in that they are in quantitative structural accord with experiment and promotes confidence in using the model to interrogate the mechanical properties and provide reliable data for experiment.

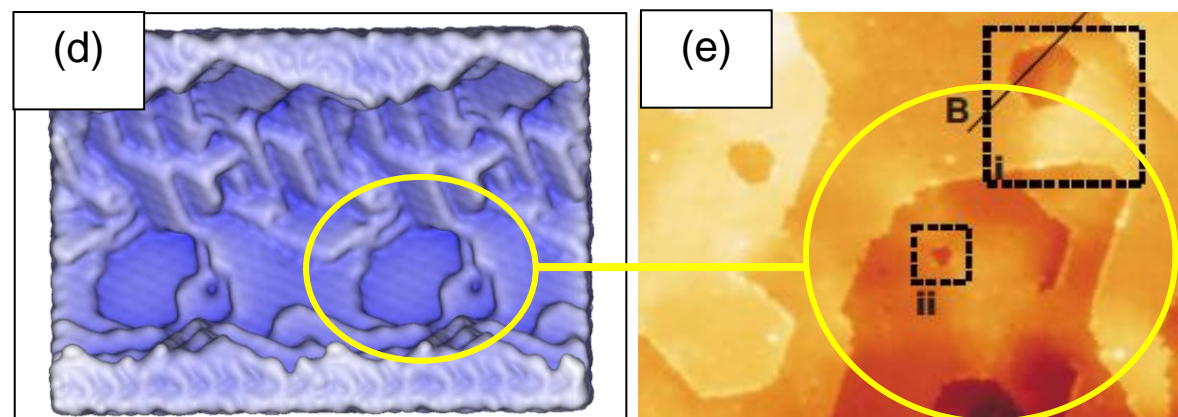
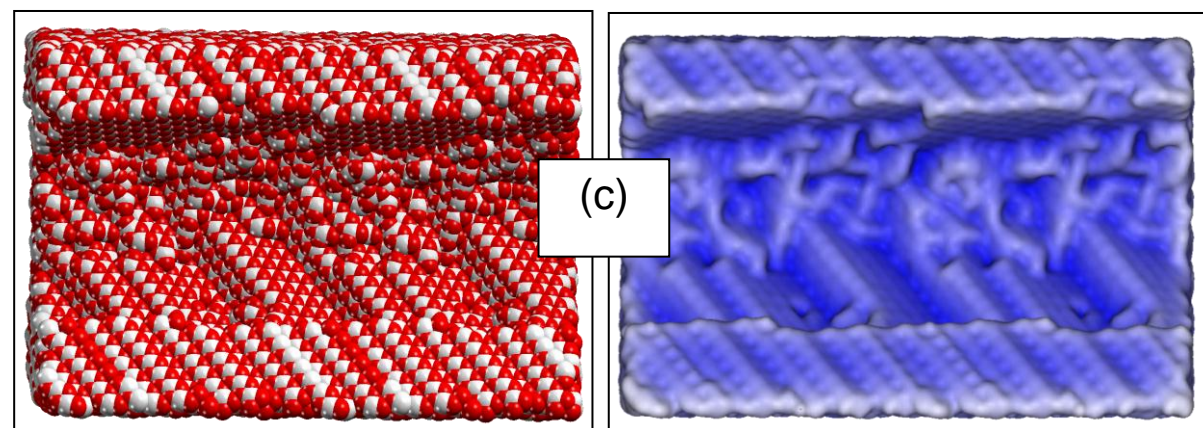
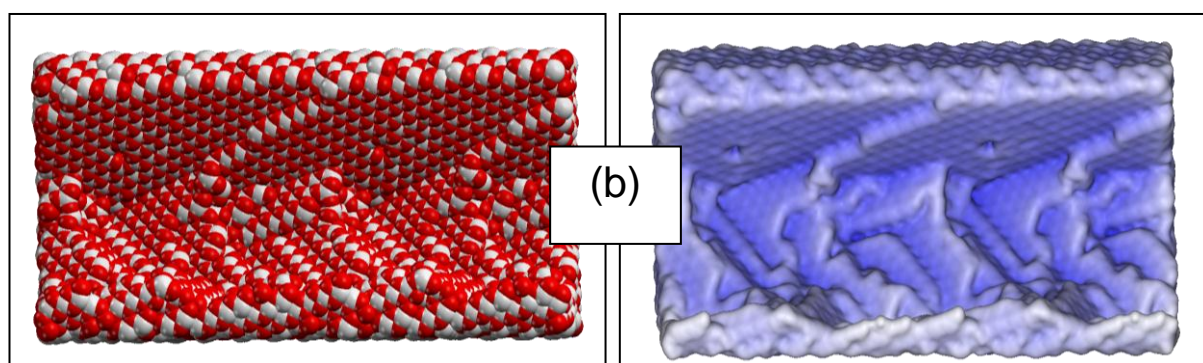
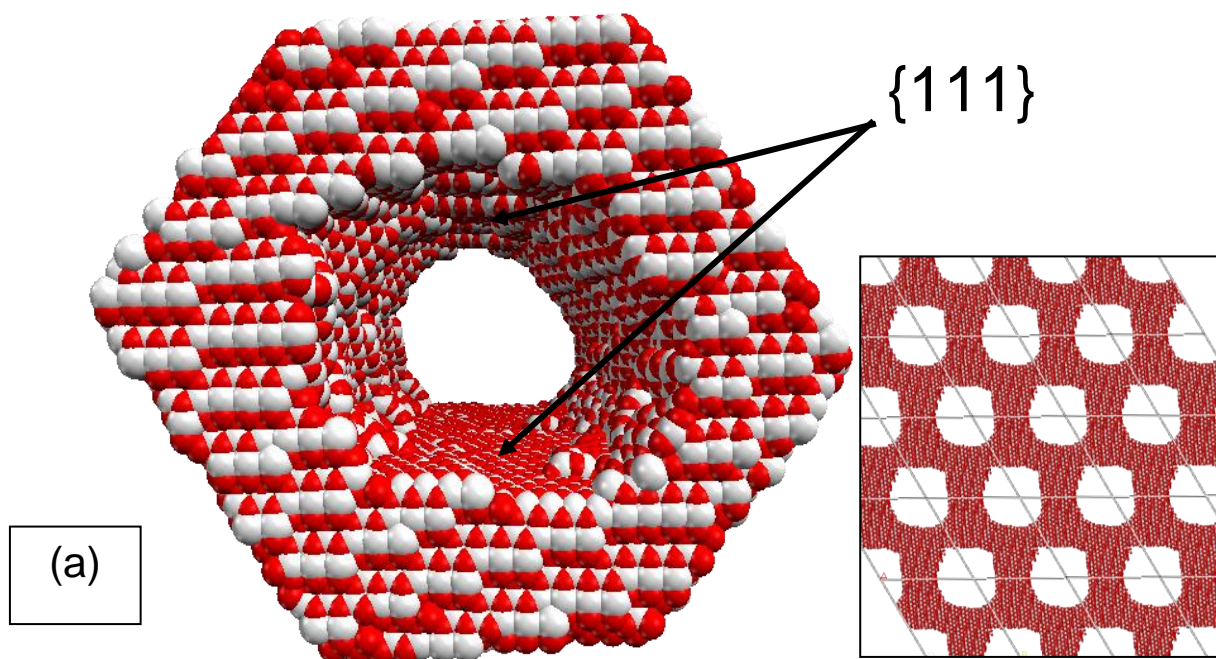


Figure 6 Characterisation of the internal pore surfaces of the ceria comprising a hexagonal array of 1D pores. (a) Perspective view looking along one of the pores, which has a (pseudo) hexagonal cross-section with $\{111\}$ exposed at the top and bottom surfaces. (b,c) Sphere model representation (left) and surface rendered model (right) of the pore surfaces revealing faceting of the surfaces into predominantly $\{111\}$. (d) Surface rendered view of the model system, which can usefully be compared with experiment (e) having similar surface topography with hexagonal shaped pits (taken with permission from ref [14] AIP Publishing LLC copyright 2008. Cerium is coloured white and oxygen is red.

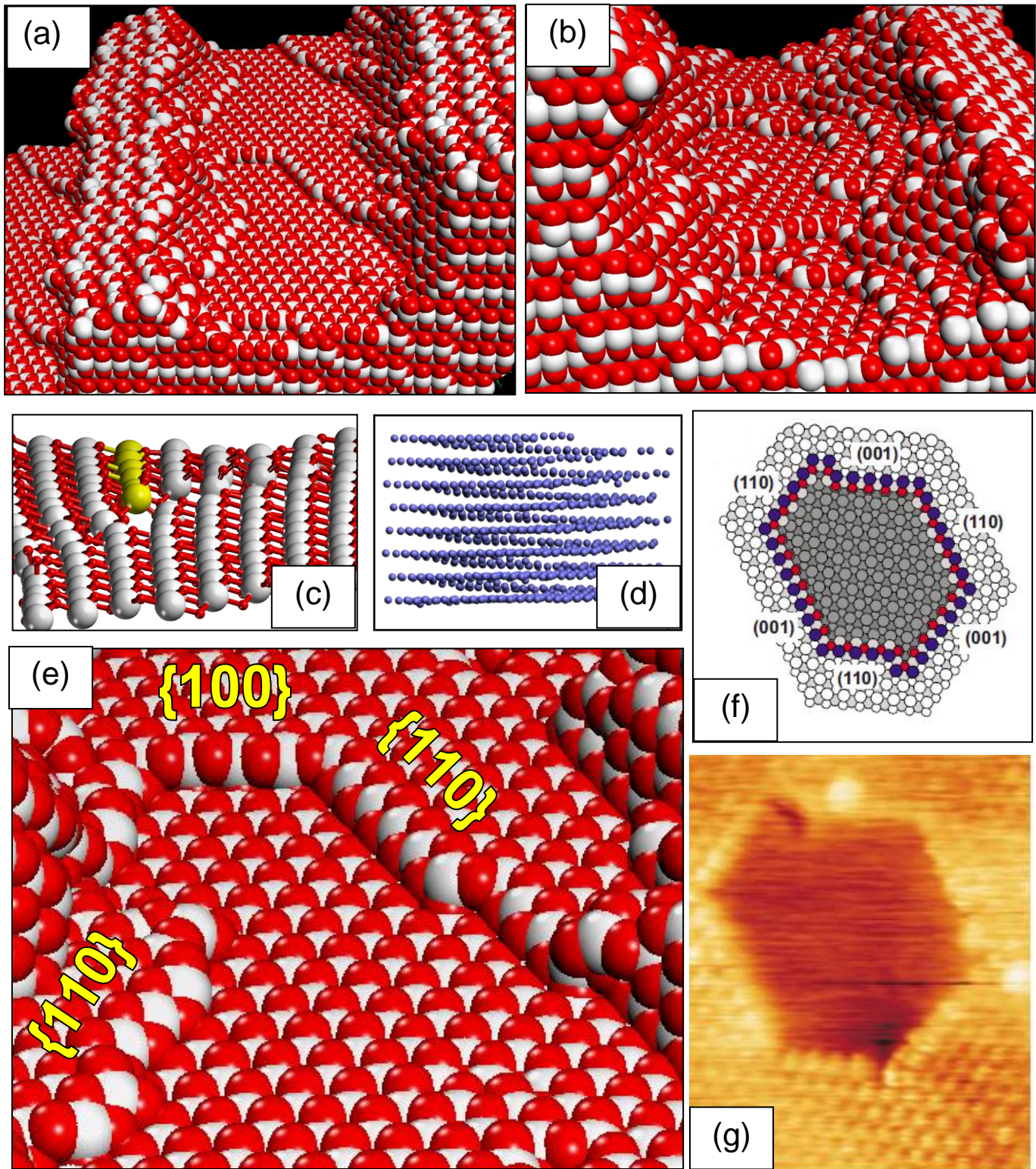


Figure 7 Characterisation and comparison with experiment of the internal pore surfaces of the ceria model with hexagonal array of 1D pores, which includes a screw-edge dislocation running through the pore wall. (a) Perspective view of the surface of the pore. (b) Underside of the pore shown in (a). (c) Edge and (d) screw components of the dislocation. A pit, observed experimentally, (f,g), on a ceria {111} surface is characterised to have a step of three atomic layers and bounded by {110} and {100} microfacets, which is in quantitative accord with the atomistic model in that the model also comprises a hexagonal pit bounded by {110} and {100} microfacets with a step height of three atomic layers, shown in (e). Cerium is coloured white and oxygen is red. Experimental data taken from ref. [14] AIP Publishing LLC copyright 2008.

Mechanical Properties

Calculated stress-strain curves for the nanoporous ceria architectures, in response to mechanical load, were used to extract the yield stress/yield strain and elastic moduli, and are reported, in table 1 and fig 8. Experimentally measure values [¹⁵] are also reported in table 1 together with density functional theory calculations on fully dense ceria [¹⁶].

Table 1 Mechanical properties of nanoporous ceria with hexagonal or cubic array of 1D pores; the load directions of the nanoporous ceria are defined in figure 2.

Pore Structure	Load Axis	Compression		Tension		Elastic Modulus GPa
		Yield Strain %	Yield Stress GPa	Yield Strain %	Yield Stress GPa	
Cubic Pores (Grain-Boundary)	<u>a</u>	-6	5.4	3	-2.1	99
	<u>b</u>	-8	9.6	5	-4.5	102
	<u>c</u>	-7	13.8	7	-8.1	162
Hexagonal Pores (No dislocation)	<u>a</u>	-7	5.1	5	-3.9	84
	<u>b</u>	-4	6.9	4	-4.2	138
	<u>c</u>	-10	20.1	5	-6.6	171
Hexagonal Pores (Dislocation)	<u>a</u>	-7	6	6	-4.2	84
	<u>b</u>	-3	3	5	-3.3	114
	<u>c</u>	-9	16.2	6	-7.8	165
Bulk CeO ₂ This work					215	
Bulk CeO ₂ DFT Ref. [16]			22.7, (0.5)		227	
Bulk CeO ₂ Experiment Ref. [15]			0.25		175	

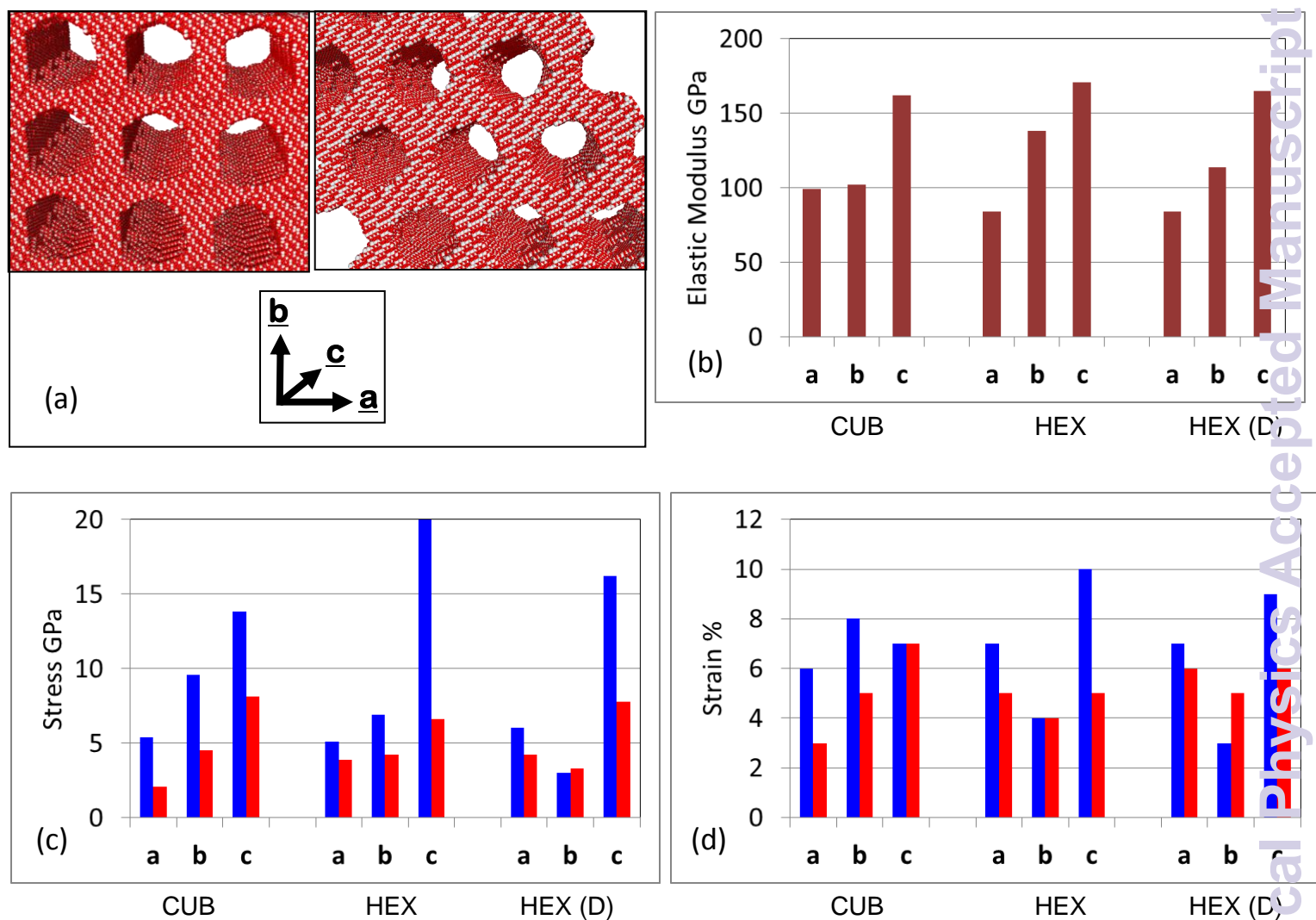


Fig. 8 Mechanical properties of nanoporous ceria as a function of nanoarchitecture. (a) atomistic models with (left) cubic (CUB) and hexagonal (HEX) array of 1D pores together with the loading directions. (b) Calculated elastic moduli. (c) Calculated yield stress. (d) Calculated yield strain. HEX(D) indicates the hexagonal pore system, which includes a dislocation, fig. 7. Bars coloured blue correspond to uniaxial compression, and bars coloured red correspond to uniaxial tension.

Stress-strain curves, for the hexagonal pore system without dislocation under uniaxial compression, fig. 9, reveal near linear elastic regions followed by plastic deformation and collapse of the nanoarchitecture. The figure also reports the stress-strain curves in directions perpendicular to the uniaxial stress applied to the system. For example, fig. 9(a)

reveals that compressing the hexagonal pore system along **a** (blue trace) results in stress and subsequent expansion along **c** (green trace). Specifically, a compressive stress, within the elastic limit, of 5.1 GPa along **a** results in a 7% contraction of the lattice along **a**. To help mitigate the stress within the system, the lattice expands by about 1% along **c** (green trace). Conversely, no expansion/contraction along **b** was observed (red trace). Similarly, a compressive stress of 6.9 GPa along **b**, fig 9(b), results in a 4% contraction along **b** (red trace) and in response, the system expands along **a** (blue trace) and **c** (green trace) by 4 and 1%, respectively, fig 9(b). The mechanical response to load is therefore highly anisotropic for the hexagonal pore architecture under uniaxial load acting along **a** and **b**. However, uniaxial load along **c** results in an isotropic response in perpendicular directions. Specifically, 20.1 GPa of compressive stress along **c**, fig 9(c), results in a 10% contraction along **c** and 3% (isotropic) expansion along both **a** and **b**.

The expansions/contractions of the lattice in directions perpendicular to the uniaxial load directions are given in table 2 and were used to extract Poisson ratios, table 2. Poisson's ratio for ceria is ca. 0.3 [17]. A review of Poisson's ratios and its implications are reviewed in ref. [18].

Poisson's ratios were calculated, at the elastic limit, for directions normal to the load direction as the change in length of the nanoporous ceria normal to the load direction divided by the change in length of the nanoporous ceria parallel to the load direction.

Table 2 Yield strains and Poisson ratios, normal to the direction of the applied load for nanoporous ceria with hexagonal or cubic array of 1D pores; the load directions of the nanoporous ceria are defined in figure 2.

		Yield Strain (%)						Poisson Ratio					
		Compression			Tension			Compression			Tension		
Pore Structure	Load Axis	<u>a</u>	<u>b</u>	<u>c</u>	<u>a</u>	<u>b</u>	<u>c</u>	<u>a</u>	<u>b</u>	<u>c</u>	<u>a</u>	<u>b</u>	<u>c</u>
Cubic Pores (Grain-Boundary)	<u>a</u>	-6	1	1	3	-0.3	-0.3		0.2	0.2		0.1	0.1
	<u>b</u>	1	-8	1	-0.5	5	-0.5	0.1		0.1	0.1		0.1
	<u>c</u>	2	2	-7	-2	-1	7	0.3	0.3		0.3	0.1	
Hexagonal Pores (No Dislocation)	<u>a</u>	-7	0	0.7	5	0	-0.5		0.0	0.1		0.0	0.1
	<u>b</u>	3	-4	1	-1.8	4	-0.7	0.8		0.3	0.5		0.2
	<u>c</u>	3	3	-10	-1	-1	5	0.3	0.3		0.2	0.2	
Hexagonal Pores (Dislocation)	<u>a</u>	-6	0.5	0.5	5	0	-0.5		0.1	0.1		0.0	0.1
	<u>b</u>	1	-2	0.4	-1	4	-0.5	0.5		0.2	0.3		0.1
	<u>c</u>	2	2	-8	-1	-2	6	0.3	0.3		0.2	0.3	

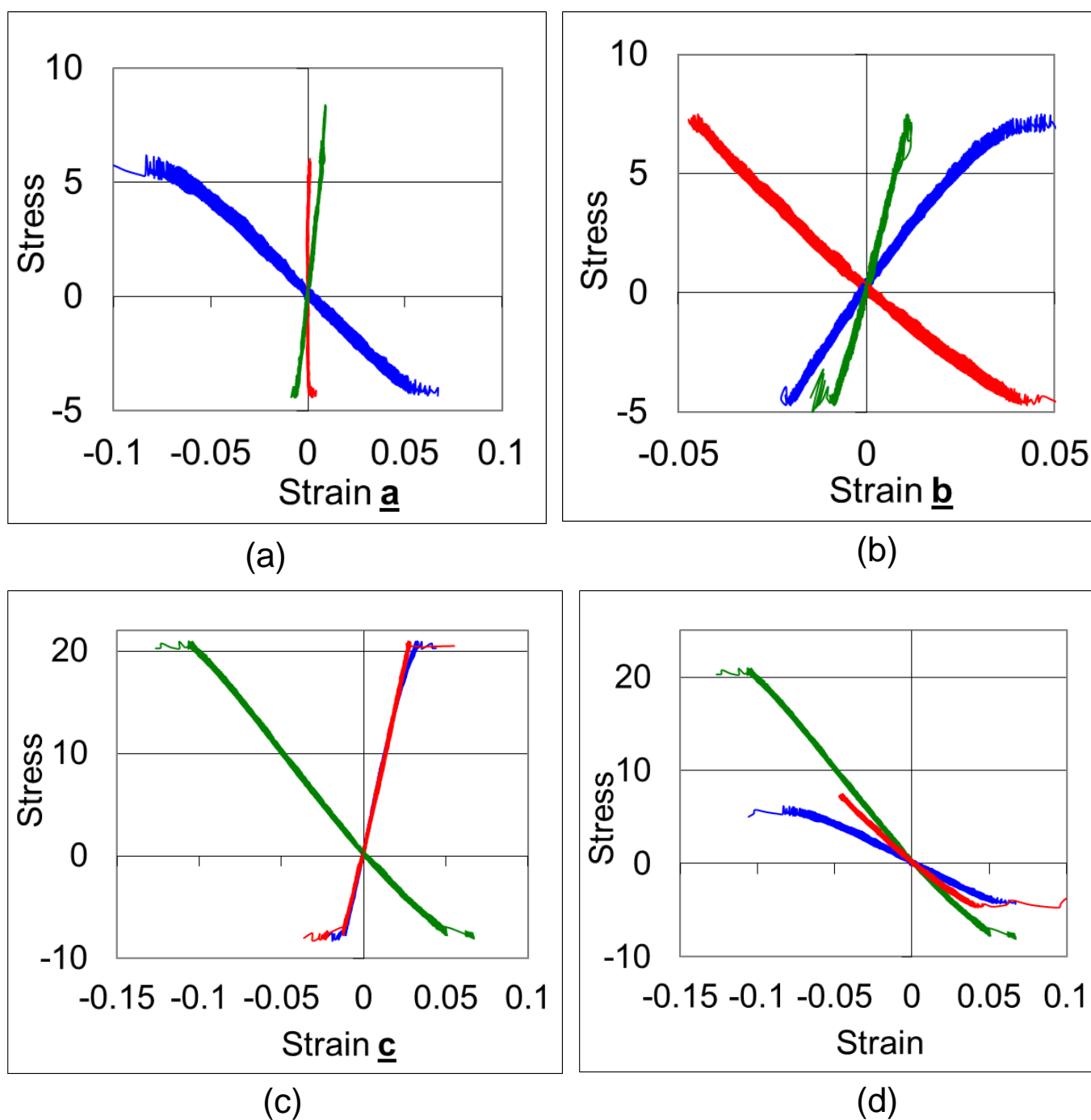


Figure 9 Calculated stress-strain curves for nanoporous ceria comprising a hexagonal array of 1D pores without screw-edge dislocation (stress in GPa). (a) Stress-strain curve for uniaxial compression and tension along a (blue trace) and corresponding strain response to the primary uniaxial load direction along b (red trace) and c (green trace) superimposed. Analogous stress-strain curves for uniaxial load imposed along b and c are shown in (b) and (c). (d) Stress-strain curves for uniaxial load directions a, b and c superimposed. Colour notation: Blue: stress-strain trace along a; Red: stress-strain trace along b; green: stress-strain trace along c.

Deformation mechanisms

Molecular graphics animations were used to analyse the atomistic models, under uniaxial compression and tension, to elucidate the deformation mechanisms; the structural responses to compressive load for the hexagonal and cubic pore systems are shown graphically in fig 10.

Cubic Pore System

Compression of the nanoceria comprising a cubic array of pores, fig 10(a), along either **a** or **b** is shown in fig 10(b,c). Analysis of the starting structure reveals a twin-grain boundary, as evidenced by ABA stacking, fig 11(a), of the cerium sublattice. Under compression, along **a**, the twin boundary grows out via a twinning dislocation moving in the plane of the grain boundary, fig 11(b), and the material deforms plastically via a change from ABA to ABC stacking of the cerium sublattice, fig 11(c).

Imposing tensile load along **c** results in crack formation. Analysis of the system, using molecular graphics, reveals the presence of point defects on one of the {111} surfaces of the pores, fig 12(a,b), which nucleates fracture of the lattice exposing two {111} fracture surfaces, fig 12(c).

We also note that tensioning the system comprising cubic pores along **c** results in a fluorite-to-rutile phase change, fig.12 (d,e). This has been predicted, using atomistic simulation, previously by us for ceria nanorods, which extend along [110] as the primary axis [¹⁹]. The phase change facilitates stress relief as the rutile-structured polymorph is associated with a reduced density.

Hexagonal Pore System

For the system comprising a hexagonal array of pores (no dislocation), fig 10(d), plastic deformation under compression along **b**, proceeds via the evolution of a crack leading to a flattening of the 1D pores, fig 10(e). Conversely, plastic deformation under compression along **a**, proceeds via a slip mechanism, fig 10(f) again resulting in a collapse of the pores.

For the system comprising a hexagonal array of pores together with intrinsic dislocations under compression along **b** reveals two yield points, fig 13(a). In particular, the system yields at about 3 GPa/0.03 and deforms plastically via dislocation glide, fig 12(c,d), to 5% strain whereupon the dislocation is annihilated at the free (internal) surface and the material deforms elastically again to 8% strain (yield strength of 7 GPa). The system then deforms plastically, driven by a dislocation, which evolved at the surface of the pore and nucleated via a surface imperfection. We note that the elastic modulus increases by about 20% after the dislocation is annihilated.

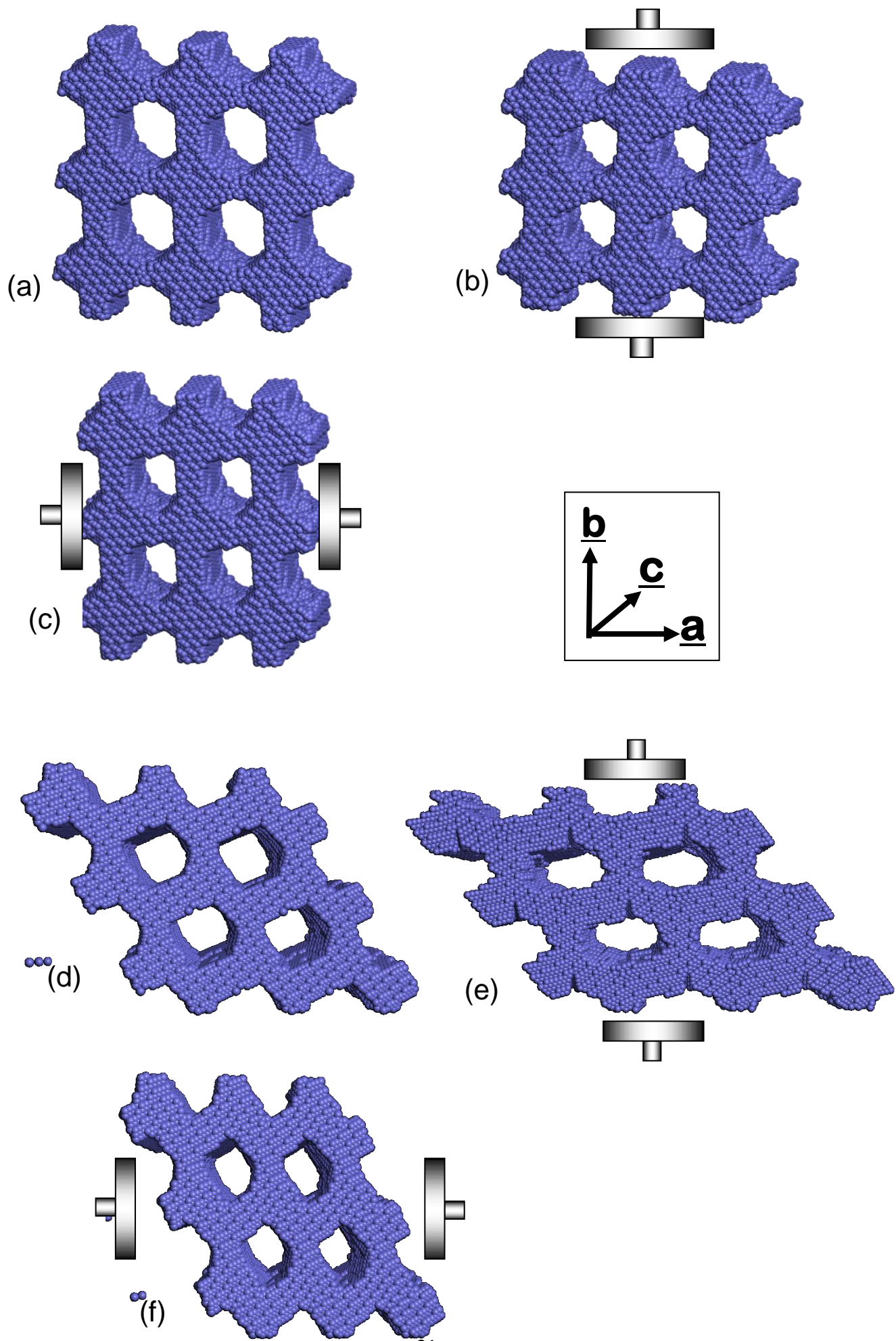


Figure 10 Structural response of the cubic and hexagonal pore systems under compression. (a) cubic pore system at the start of the simulation, (b) after plastic deformation under compressive load along **b** and (c) after plastic deformation under compressive load along **a**. (d) Hexagonal pore system at the start of the simulation, (e) after plastic deformation under compressive load along **b** and (f) after plastic deformation under compressive load along **a**. Cerium atom positions are represented by the blue spheres; oxygen atoms are not shown.

DISCUSSION

A comparison between the yield strength of the hexagonal pore system with and without dislocation reveals that the system is weakened by the presence of a screw-edge dislocation under compression. In particular, the compressive yield stress/strain is reduced from 6.9GPa/-0.04 to 3.0GPa/-0.03 (uniaxial compression along **b**); the elastic modulus is also reduced from 138 to 114GPa, table 1. Conversely, under compression along **a** or **c**, the yield strengths of the system with or without a dislocation are similar; the yield strength (tension) is much less influenced by the dislocation. The crystal structure governs such behaviour – specifically, the direction of the compressive load with respect to the Burgers vector of the dislocation, fig 13(c,d). The mechanical properties are therefore critically dependent upon the orientation of the pore direction with respect to the crystal direction and the load direction.

The orientational relationship between the pore direction and crystal direction emanates from the embryonic stages of crystallisation, fig 4, and therefore our simulations predict that the mechanical properties of nanoporous materials are tuneable by controlling the synthetic conditions when fabricating the real material. This may include, for example, modifying the solvent and pH to stabilise particular ceria surfaces and morphologies [20], templating agents [21, 22], temperature [23].

Dislocations provide vehicles for plastic deformation. If the material does not comprise an intrinsic dislocation, the system can only deform plastically when the applied load is sufficiently high to evolve a dislocation. Our calculations reveal that the compressive stress required to evolve a dislocation and facilitate plastic deformation in nanoporous ceria is

twice the stress required to plastically deform the same system that already includes a dislocation (table 1, hexagonal pore system, loading along **b**). In particular, in our system, a surface vacancy cluster, fig 12(b), nucleated the evolution of a dislocation enabling plastic deformation; oxygen vacancies are created in reduced ceria (CeO_{2-x}) to facilitate charge neutrality associated with Ce(IV) - Ce(III) transitions and therefore we predict that reduced ceria will be less resilient to mechanical stress because there will likely be a higher concentration of surface imperfections to nucleate dislocation or crack evolution.

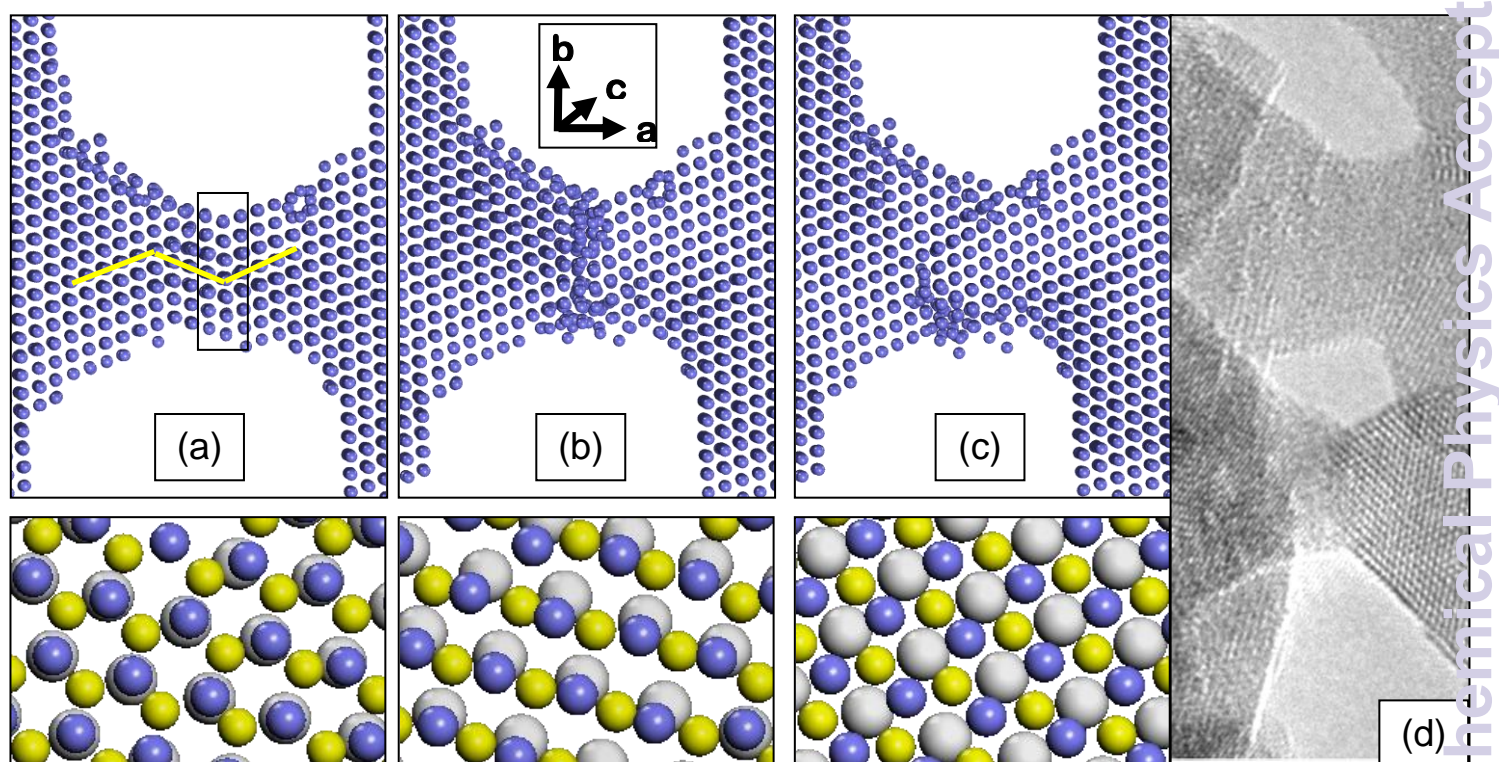


Figure 11 Plastic deformation mechanisms, of the nanoporous ceria with cubic array of 1D pores, in respond to load acting along **a**. (a) top: view depicting the cell wall of the nanoarchitecture (only cerium atoms, coloured blue, are shown); bottom: ABA stacking of the cerium sublattice associated with the nanotwin grain-boundary (cerium atoms are coloured to differentiate cerium in each of the three layers ABA stacking -A(blue), B(yellow), A(white). (b) Top: as (a) but after the system has started to plastically deform under compressive stress; bottom: 'partial' transformation of ABA stacking to ABC stacking. (c) Top: after the system has plastically deformed eliminating the grain-boundary facilitating ABC stacking (bottom). (d) Comparison with the real mesoporous material, reproduced with permission from ref. [12] copyright (2013) American Chemical Society.

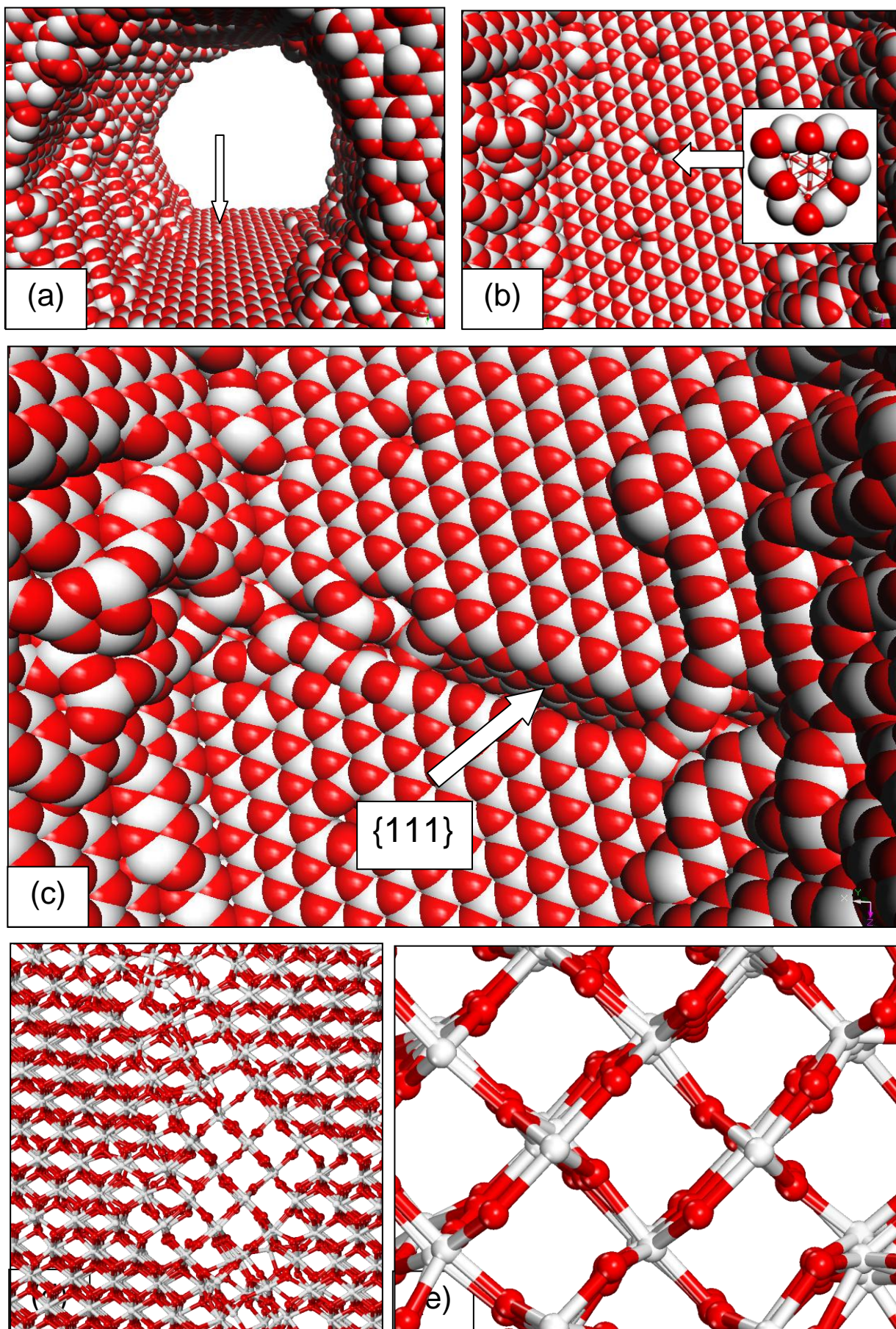


Figure 12 Atomistic models of nanoporous ceria, with cubic array of 1D pores, under uniaxial tension (along \underline{c}) revealing crack formation and a fluorite-rutile phase change. (a) View looking along the pore revealing point defects that have evolved on the $\{111\}$ surface. (b) Enlarged view of (a) showing more clearly the atomistic structure of a point defect cluster (inset). (c) View looking along $\langle 111 \rangle$ revealing crack evolution, which nucleates at the position of the point defects. The fracture plane is $\{111\}$ as evidenced by the exposure of two $\{111\}$ surfaces. (d) Segment of the nanoporous ceria, which has transformed from a fluorite to a rutile phase. (e) Enlarged segment of (d) showing more clearly the rutile phase.

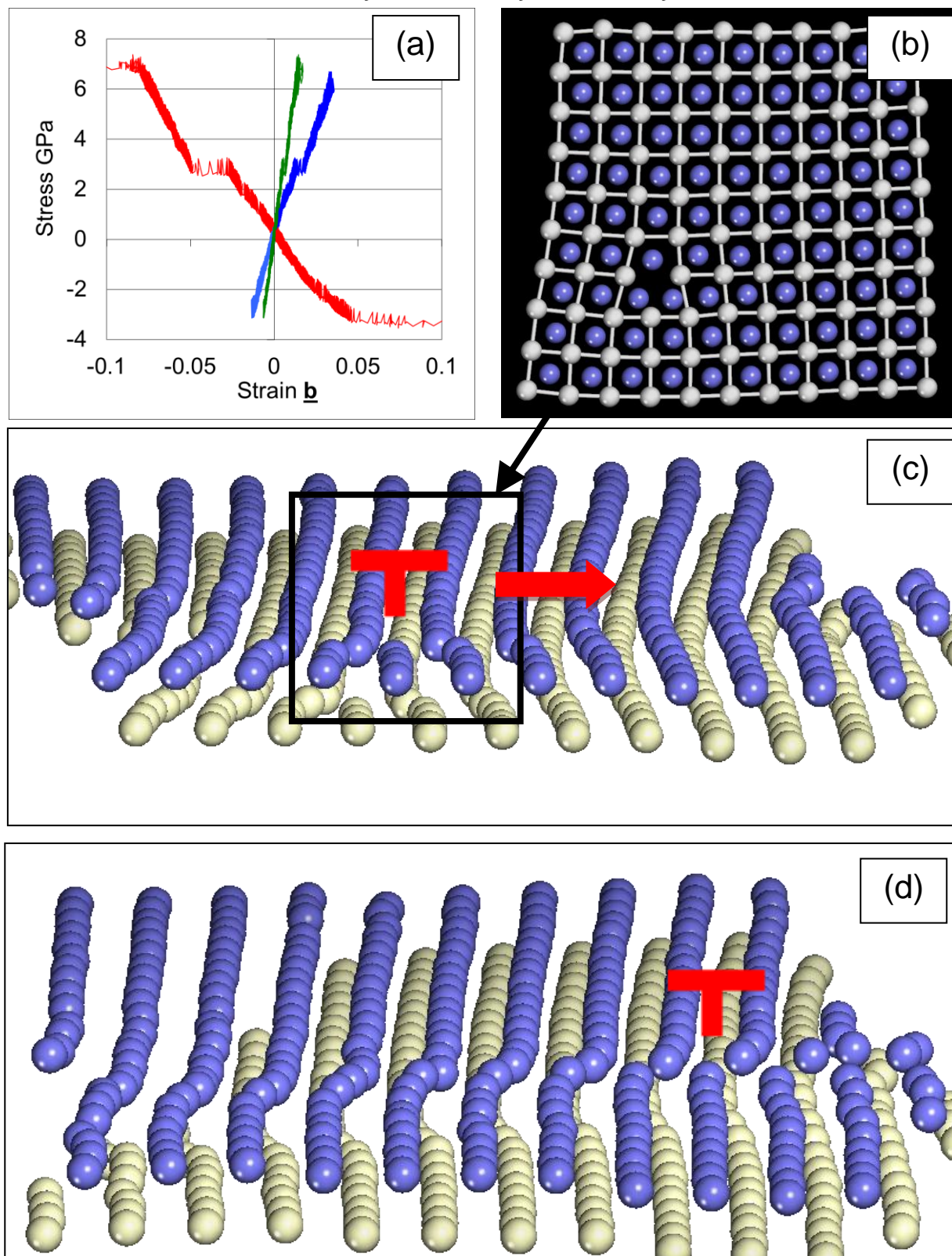


Figure 13 Plastic deformation of the hexagonal pore system, which includes a dislocation. (a) stress-strain curve of the system under uniaxial load along \underline{b} . (b) atomistic structure of the dislocation. (c,d) atomistic structure of the core region of the dislocation showing dislocation glide under compression; the dislocation moves from left, (c), to right, (d). Cerium atoms in two neighbouring atomic layers are shown coloured blue and white; oxygen is not shown to improve clarity. The edge component is highlighted by the red 'T'.

Poissons ratios

Our calculations reveal that for the cubic pore system, the expansion/contraction of the lattice perpendicular to the primary load direction is predominantly isotropic. Conversely, the hexagonal pore system exhibits a predominantly anisotropic response. Specifically, compression of the hexagonal array of 1D pores along **b** results in a substantial expansion along **a**. This is because the compressive forces along **b** are resolved with components along **a** as the stress cannot be communicated through the void, fig 14(a); compression along **a** has no effect on the expansion along **b** because the forces can act continuously along **a** without resolving a component of the force along **b**. Similarly, we might expect the elastic modulus along **a** to be greater than **b**. However, our calculations reveal, table 1, that the elastic modulus along **b** is 60% greater than along **a**. Atomistic simulation can therefore provide additional insight to continuum mechanical approaches, which are more commonly used to elucidate the mechanical properties of a material [24]. In particular, forces are communicated via atom-atom bonds and bond angles. Accordingly, the mechanical properties will depend critically upon the orientational relationship between the crystal direction with respect to the pore direction and an atomistic model is needed to reliably predict the mechanical properties.

We caution that our reported expansions/contractions of the lattice and hence Poissons ratios are perhaps disingenuous because such (an)isotropy is a result of the arbitrarily chosen primary load direction. For example, compression along the **ab**-direction for nanoporous ceria with cubic array of 1D pores, fig. 2 (d), as the primary load direction would likely deliver anisotropic behaviour perpendicular to the direction of the applied load as discussed for the hexagonal pore system above. Accordingly, similar to the 'rules of crystallography', the loading directions of a nanoarchitecture need to be defined to enable robust comparison between architectures. Nomenclature is therefore required to define the loading, pore and crystal directions together with the orientational relationship between them.

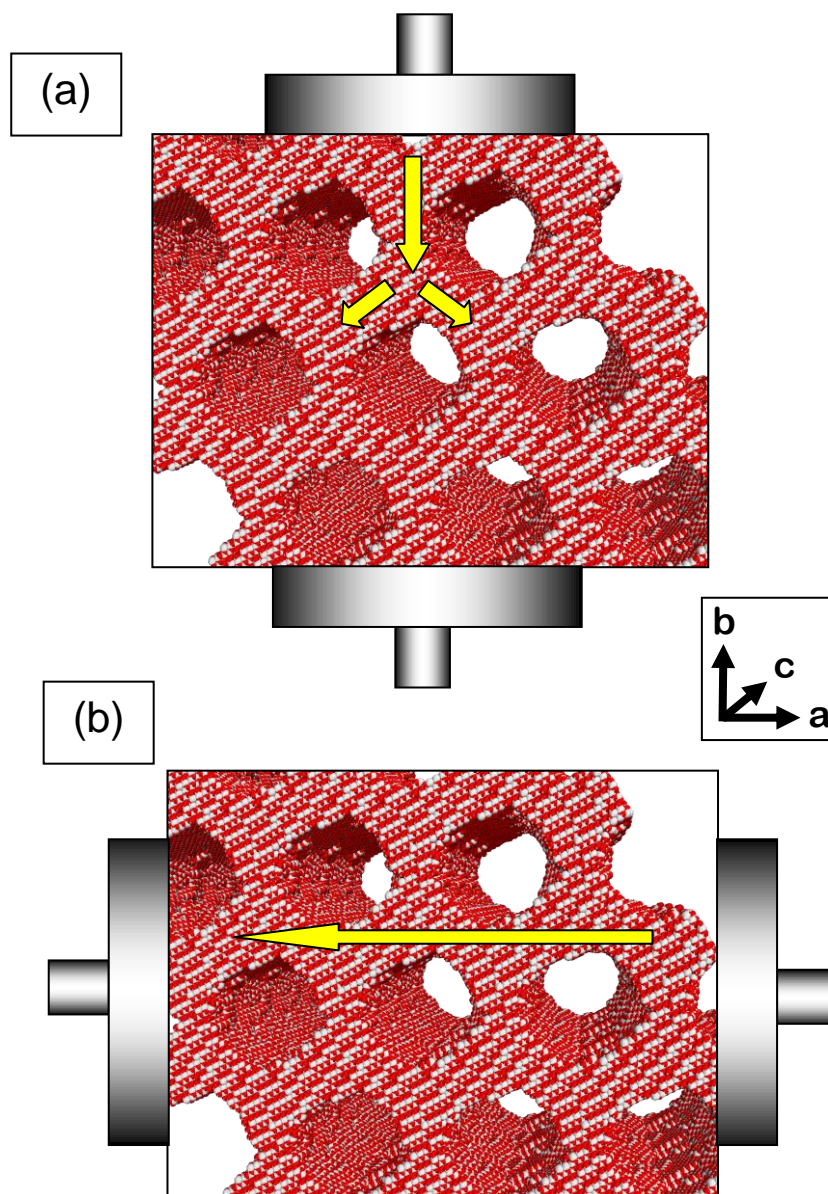


Fig 14 Forces acting on nanoporous ceria comprising a hexagonal array of 1D pores. Top: compression along \underline{b} results in the forces being resolved in both \underline{a} and \underline{b} to circumnavigate the void. Bottom: compression along \underline{a} does not require the forces to be resolved.

The complexity is further compounded when one considers extended defects with respect to the pore (symmetry). For example, fig 2(e) (inset) appears to show the existence of a stacking fault in the array of pores, which would likely influence the mechanical properties.

This epitomises the hierarchical structural complexity than one must address to have a coherent understanding of the mechanical properties of nanoporous functional materials including: crystal structure, microstructure (dislocations, grain-boundaries, point defects, morphology of internal pores) and pore structure (pore symmetry and connectivity) together with the orientational relationships between these hierarchical structural levels. We also note that microstructural ‘defects’ at the pore level of hierarchical structure, fig. 2(e) (inset), also need to be included.

Sakanoi and co-workers used density functional theory to calculate the Young's modulus (221.8 GPa) and fracture strength (22.7 GPa) of CeO_2 [16]. This compares with 175 GPa (Young's Modulus) and 0.25 GPa (fracture strength) measured experimentally. They attributed the difference in fracture strength to the presence of cracks that were not included in the structural model; combined with Griffith theory, which modifies the ideal fracture strength as a function of crack length (taken as 20 μm), they predicted that the fracture strength reduces to 0.47 GPa – in close accord with experiment. For a nanoporous oxide a crack can only traverse the thickness of the wall and therefore we predict that the fracture strength of a nanoporous material can approach the ideal strength. Indeed, the fracture strength of nanowiskers have been observed close to ideal values [25]. This may help explain why nature engineers materials that are nanoporous – to capture their ultimate strength. Accordingly, we propose that it might be possible to engineer such strength into synthetic materials via nanopatterning to fabricate pores in all three-dimensions.

We also suggest that the crystal structure is oriented with respect to the pore symmetry such that the primary slip or crack directions do not lie commensurate with the nanoframe direction to prevent a dislocation or crack traversing the nanoframe [26] rather than being annihilated at a pore. On the other hand, the existence of point and extended defects at the crystal level, and pore level, fig 2(f) (inset) would help mitigate this possibility and might help explain why porous architectures found in nature do not exhibit long-range ordering of the pore structures.

Simulating the deformation and fracture of a solid (bulk) material is difficult using MD simulation. This is because models, which exploit periodic boundary conditions, do not include a free surface; surface defects such as dislocations and cracks provide weak links for plastic deformation. Accordingly, simulations using periodic boundary conditions do not give a true reflection of the real material and the mechanical properties can be orders of magnitude different compared to the measured values. For example, in table 1, the predicted yield stress using DFT is 22.5 GPa, whereas the measured value is 0.25 GPa. However, adjustments can be made to the predicted value to give a more realistic comparison with experiment. In particular, 22.5 GPa reduces to 0.5 GPa (table 1). The adjustments are explained in detail in ref. [16]. Conversely, nanoporous materials do have (internal) surfaces and therefore the influence of surface cracks or dislocations can be captured within the simulations as we have shown in this study. Inevitably periodic boundary conditions will introduce some artificial constraints, such as one pore being slightly more resilient to stress than another (one wall comprising the nanoporous material might have a dislocation or surface crack, whereas a neighbouring wall might be pristine). However, this is likely to introduce more subtle differences compared to the orders of magnitude differences compare to simulating the parent (bulk) material. Creating models with much larger unit cells (many pores) will help mitigate the approximations that emanate from using periodic boundary conditions in the simulations, but they will, inevitably, incur much higher computational cost.

CONCLUSION

We have used molecular dynamics simulation to predict yield stresses/strains for nanoporous ceria (*comprising smaller than 10nm pores and 10nm wall thicknesses*) of up to 20.1 GPa/-10% (compression) and -8.1 GPa/7% (tension) - almost two orders of magnitude higher than the parent bulk material (0.25 GPa yield strength).

Mechanical failure (plastic deformation) is driven via dislocation and/or cracking and proceeds along characteristic slip planes or crack directions within the fluorite-structured material. Surface defects/imperfections nucleate the evolution of dislocations and cracks in the pristine (dislocation-free) system under load.

The mechanical properties are governed by the orientation between the crystal symmetry/direction and the pore symmetry/direction. Such orientational relationship emanates from the embryonic stages of crystallisation of the walls of the nanoporous

material. Our simulations predict that modifying synthetic conditions, such as solvent, pH, temperature, surfactant and/or templating agents - to exact control over the crystallisation and surfaces exposed (morphology) - can be used to tune the mechanical properties of nanoporous ceramics. The mechanical properties of a material are therefore critically dependent upon several levels of hierarchical structural complexity including: the crystal structure, microstructure (including: dislocations, grain-boundaries, morphology), pore structure. Moreover, because forces can only be communicated via atom-atom bonds and bond angles, which emanate from the crystal structure and its orientation with respect to the pore symmetry, atomistic simulation can provide unique additional insight compared to continuum mechanical approaches. To calculate the mechanical properties directly, all the levels of hierarchical structural complexity must be captured in a *single* model.

Acknowledgements

EPSRC: EP/H001220/1; EP/H001298/1; EP/H005838/1

Supporting information

Animations depicting the simulated plastic deformation of the porous nanoarchitectures are available from the authors.

References

-
- ¹ Kim, Y. Y.; Ribeiro, L.; Maillot, F.; Ward, O.; Eichhorn, S. J.; Meldrum, F. C. Bio-Inspired Synthesis and Mechanical Properties of Calcite-Polymer Particle Composites *Adv. Mater.*, 2010, 22, 2082.
 - ² Lai, M.; Kulak, A. N.; Law, D.; Zhang, Z. B.; Meldrum, F. C. and Riley, D. J. Profiting from nature: macroporous copper with superior mechanical properties *Chem. Commun.*, 2007, 34, 3547-3549.
 - ³ Shan, Z. W.; Adesso, G.; Cabot, A.; Sherburne, M. P.; Asif, S. A. S.; Warren, O. L.; Chrzan, D. C.; Minor, A. M. and Alivisatos, A. P. Ultrahigh stress and strain in hierarchically structured hollow nanoparticles *Nat. Mater.*, 2008, 7, 947-952.
 - ⁴ Suresh, S. and Li, J. Materials Science Deformation of the ultra-strong *Nature*, 2008, 456, 716-717.
 - ⁵ Jauffres, D; Yacou, C.; Verdier, M.; Dendievel, R. and Ayrat, A. Mechanical properties of hierarchical porous silica thin films: Experimental characterization by nanoindentation and Finite Element modeling *Micropor. Mesopor. Mat.*, 2011, 140,120-129.
 - ⁶ Lee, J. H.; Wang, L. F.; Kooi, S.; Boyce, M. C.; Thomas, E. L.; Enhanced Energy Dissipation in Periodic Epoxy Nanoframes *Nano Lett.*, 2010, 10, 2592-2597.
 - ⁷ Ren, Y.; Ma, Z. and Bruce, P. G.

- Ordered mesoporous metal oxides: synthesis and applications
Chem. Soc. Rev., 2012, 41, 4909-4927.
- ⁸ Deng, S.; Tjoa, V.; Fan, H.M.; Tan, H.R.; Sayle, D.C.; Olivo, M.; Mhaisalkar, S.; Wei, J. and Sow, C.H.
Reduced Graphene Oxide Conjugated Cu₂O Nanowire Mesocrystals for High-Performance NO₂ Gas Sensor
J. Am. Chem. Soc., 2012, 134, 4905-4917.
- ⁹ Sayle, T. X. T.; Parker, S. C. and Catlow, C. R. A.
The role of oxygen vacancies on ceria surfaces in the oxidation of carbon monoxide
Surf. Sci., 1994, 316, 329-336.
- ¹⁰ Smith, W.; Forester, T. R.
DL_POLY, copyright by the council for the Central Laboratory of the Research Councils, Daresbury Laboratory, Daresbury, Warrington, UK (1996)
http://www.stfc.ac.uk/CSE/randd/ccg/software/DL_POLY/25526.aspx
- ¹¹ Deshpande, A.S.; Pinna, N.; Smarsly, B.; Antonietti, M. and Niederberger, M.
Controlled assembly of preformed ceria nanocrystals into highly ordered 3D nanostructures
Small, 2005, 1, 313-316.
- ¹² Pascal Hartmann, Torsten Brezesinski, Joachim Sann, Andriy Lotnyk, Jens-Peter Eufinger, Lorenz Kienle, and Jürgen Janek
Defect Chemistry of Oxide Nanomaterials with High Surface Area: Ordered Mesoporous Thin Films of the Oxygen Storage Catalyst CeO₂-ZrO₂
ACS Nano, 2013, 7 (4), pp 2999-3013
- ¹³ Conesa, J. C.
Computer modelling of surfaces and defects in ceria
Surf. Sci., 1995, 339, 337-352.
- ¹⁴ Torbruegge, S.; Cranney, M. and Reichling, M.
Morphology of step structures on CeO₂(111)
Appl. Phys. Lett., 2008, 93, 073112.
- ¹⁵ Sato, K.; Yugami, H. and Hashida, T.
Effect of rare-earth oxides on fracture properties of ceria ceramics
J. Mater. Sci., 2004, 39, 5765-5770.
- ¹⁶ Sakanoi, R.; Shimazaki, t.; Xu, J.; Higuchi, Y.; Ozawa, N.; Sato, K.; Hashida, T. and Kubo, M
Different behavior of Young's modulus and fracture strength of CeO₂: Density functional theory calculations
J. Chem. Phys., 2014, 140, 121102-1-4
- ¹⁷ Mogensen, M.; Sammes, N. M. and Tompsett, G. A.
Physical, chemical and electrochemical properties of pure and doped ceria
Solid State Ionics, 2000, 129, 63-94.
- ¹⁸ Greaves, G. N.; Greer, A. L.; Lakes, R. S. and Rouxel, T.
Poisson's ratio and modern materials
Nat. Mater., 2011, 10, 823-827.
- ¹⁹ Sayle, T. X. T. and Sayle, D. C.
Elastic Deformation in Ceria Nanorods via a Fluorite-to-Rutile Phase Transition
ACS Nano, 2010, 4, 879-886.
- ²⁰ Molinari, M., Parker, S.C., Sayle, D.C. and Islam, M.S.
Water Adsorption and Its Effect on the Stability of Low Index Stoichiometric and Reduced Surfaces of Ceria
J. Phys. Chem. C. 2012, 116, 7073-7082.
- ²¹ Ji, P.; Zhang, J.; Chen, F. and Anpo, M.
Ordered Mesoporous CeO₂ Synthesized by Nanocasting from Cubic Ia3d Mesoporous MCM-48 Silica: Formation, Characterization and Photocatalytic Activity
J. Phys. Chem. C, 2008, 112, 17809-17813.
- ²² Green, D. C.; Glatzel, S.; Collins, A. M.; Patil, A. J. and Hall, S. R.
A New General Synthetic Strategy for Phase-Pure Complex Functional Materials
Adv. Mater., 2012, 24, 5767-5772.
- ²³ Feng, X. D.; Sayle, D. C.; Wang, Z. L.; Paras, M. S.; Santora, B.; Sutorik, A. C.; Sayle, T. X. T.; Yang, Y.; Ding, Y.; Wang, X. D. and Her, Y. S.
Converting ceria polyhedral nanoparticles into single-crystal nanospheres
Science, 2006, 312, 1504-1508.
- ²⁴ Guz, I.A. J. Nanomater Mol Nanotechnol 2012,
Continuum Solid Mechanics at Nano-Scale: How Small Can It Go?

doi:10.4172/2324-8777.1000e103

²⁵ Zhu, T. and Ju Li, J.

Ultra-strength materials

Prog. Mater. Sci., 2010, 55, 710-757

²⁶ Kermode, J. R.; Ben-Bashat, L.; Atrash, F.; Cilliers, J. J.; Sherman, D. and De Vita, A.

Macroscopic scattering of cracks initiated at single impurity atoms

Nature Communications 2013, 4, 2441.